Journal of Zhejiang University SCIENCE A
ISSN 1673-565X (Print); ISSN 1862-1775 (Online)
www.zju.edu.cn/jzus; www.springerlink.com
E-mail: jzus@zju.edu.cn

An in-plane low-noise accelerometer fabricated with an improved process flow*

Xu-dong ZHENG†, Zhong-he JIN†‡, Yue-lin WANG, Wei-jun LIN, Xiao-qi ZHOU

(*Department of Information Science and Electronic Engineering, Zhejiang University, Hangzhou 310027, China*)

†E-mail: brucezen@gmail.com; jinzh@zju.edu.cn

Received Oct. 31, 2008; Revision accepted Jan. 21, 2009; Crosschecked Aug. 14, 2009

Abstract: We present a bulk micromachined in-plane capacitive accelerometer fabricated with an improved process flow, by etching only one-fifth of the wafer thickness at the back of the silicon while forming the bar-structure electrode for the sensing capacitor. The improved flow greatly lowers the footing effect during deep reactive ion etching (DRIE), and increases the proof mass by 54% compared to the traditional way, resulting in both improved device quality and a higher yield rate. Acceleration in the *X* direction is sensed capacitively by varying the overlapped area of a differential capacitor pair, which eliminates the nonlinear behavior by fixing the parallel-plate gap. The damping coefficient of the sensing motion is low due to the slide-film damping. A large proof mass is made using DRIE, which also ensures that dimensions of the spring beams in the *Y* and *Z* directions can be made large to lower cross axis coupling and increase the pull-in voltage. The theoretical Brownian noise floor is 0.47 μg/Hz$^{1/2}$ at room temperature and atmospheric pressure. The tested frequency response of a prototype complies with the low damping design scheme. Output data for input acceleration from −1 g to 1 g are recorded by a digital multimeter and show very good linearity. The tested random bias of the prototype is 130 μg at an averaging time of around 6 s.

Key words: MEMS accelerometer, Deep reactive ion etching (DRIE), Footing effect, Capacitive sensing
doi:10.1631/jzus.A0820757 **Document code:** A **CLC number:** TN304.12

INTRODUCTION

Micro-electro-mechanical system (MEMS) accelerometers have already been widely used in automobile industry and consuming electronics, while inertial navigation, space microgravity applications and seismometry require better performances for resolution, stability, and reliability. High resolution can be achieved by reducing Brownian noise and increasing the mechanical sensitivity of a MEMS accelerometer (Yazdi and Najafi, 1997). Brownian noise can be reduced by increasing the proof mass of an accelerometer and lowering the damping coefficient for its sensing motion, while the mechanical sensitivity can be improved by reducing its mechanical resonant frequency. A low resonant frequency can be achieved by adopting a small spring constant and a large proof mass. However, the spring constant cannot be made too small due to material properties, geometric constraints, and self resonance of the spring beam (Boser and Howe, 1996), and moreover, a low resonant frequency implies a low device bandwidth for an open-looped accelerometer. Overall, a large proof mass helps both in reducing Brownian noise and in increasing the mechanical sensitivity of a MEMS accelerometer.

Surface micromachining technology fabricates microstructures from deposited thin films (Bustillo *et al.*, 1998); thus, surface micromachined accelerometers usually have small proof masses and are often operated in vacuum to minimize Brownian noise (Jiang *et al.*, 2002). However, bulk micromachined accelerometers usually have large proof masses fabricated from thick substrates (Kovacs *et al.*, 1998); thus, Brownian noise can be very low at atmospheric pressure.

‡ Corresponding author

* Project (No. NCET-06-0514) supported by the Program for New Century Excellent Talents in University, China

For capacitive sensing via the varying gap between two electrode plates, there is an instinct nonlinearity (Boser and Howe, 1996). Displacement of the movable plate is often restrained within a small value to ensure linearity, which would reduce the dynamic range for an accelerometer. Moreover, sensing via the varying gap between two electrode plates indicates that the spring constant is low in the sensing direction orthogonal to the plate surfaces. Thus, the movable electrode plate could be pulled-in at small voltages (Chae *et al*., 2004). However, this instinct nonlinearity can be eliminated for capacitive sensing via the varying overlapped area of two electrode plates (Weigold *et al*., 2001), which also has the advantage of a large pull-in voltage because it senses the position signal in the direction parallel to the plate surfaces.

Deep reactive ion etching (DRIE) is used to fabricate high aspect ratio structures. There is a deficiency with DRIE; i.e., the footing effect will occur at the silicon/silicon oxide interface when DRIE continues after the silicon is etched through. This is due to the ion deflection in the etched trench (Wang *et al*., 2007). Footing effect damages the foot area of the device and is a big concern for device quality and yield rate.

We have reported in Zheng *et al*.(2008) a bulk micromachined accelerometer, which utilizes bar-structure capacitors to sense acceleration and is fabricated in a traditional way where bars and the structure are released together through DRIE (Chen *et al*., 2003). It requires a large area of the wafer to be etched through and suffers from severe footing effect. In this paper, we present a bulk micromachined capacitive accelerometer fabricated with an improved process flow. It has a large proof mass and utilizes a linear sense scheme with a low damping coefficient. Details about the structure design for the accelerometer are given in Section 2. The previous and improved process flows are explicated and compared with each other by scanning electron microscope (SEM) photos in Section 3. Section 4 discusses the method used for testing the frequency response of the accelerometer and presents test results of the frequency response. Also, the interface circuit for the accelerometer is provided, as well as the test results of linearity and bias stability.

STRUCTURAL DESIGN

The accelerometer is a typical spring-mass system (Fig.1). U-type spring beams are chosen because the arc parts of the beams are helpful for residual stress releasing. The proof mass also serves as the movable electrode of a differential capacitor pair. This is realized by etching a set of bars on the back of the proof mass, which, together with two fixed Al electrodes under them, form the differential capacitor pair (Fig.2). The overlapped area of the bars on the movable proof mass and the fixed Al electrodes on the glass varies when there exists acceleration in the *X* direction, resulting in a linear variance of capacitance.

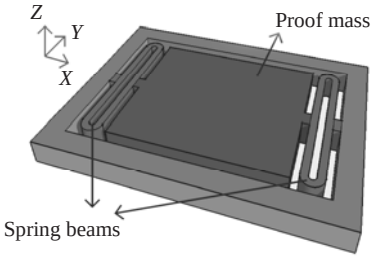

Fig.1 Structure of the accelerometer

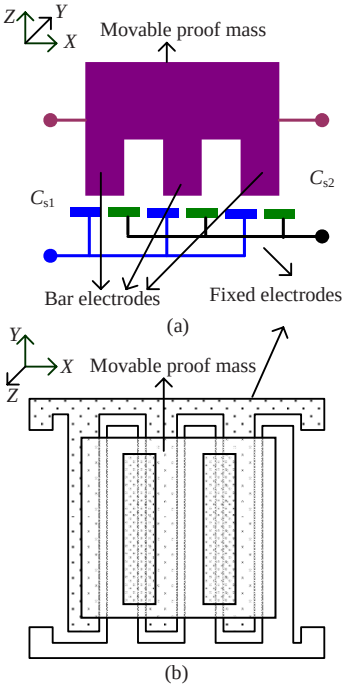

Fig.2 Differential sensing capacitor
(a) Sectional view; (b) Top view

The spring beams of the accelerometer are released via DRIE; thus, the aspect ratio of the beams is high and dimensions of the spring beams in the *Y* and *Z* directions are made large so as to reduce the cross-axis coupling. And because of the large dimensions in the *Z* direction, the pull-in voltage of the structure is very high, which implies that large sense and feedback voltages can be applied to optimize the performance of the accelerometer. The large proof mass moves in-plane while sensing acceleration, resulting in a low damping coefficient and thus a low Brownian noise floor, which is essential for high precision accelerometers.

Layout dimensions of the accelerometer are given in Table 1. W_1 and L_1 are the width and length of the four U-type spring beams, respectively; R_1 is the radius for the centerline of the arc part of the spring beams; W_2 and L_2 are the width and length of the proof mass, respectively; W_3 and L_3 are the width and length of the trenches and bars, respectively. N_1 is the number of trenches. The width and length of the fixed Al electrodes on the glass substrate are designated as W_4 and L_4, respectively.

Table 1 Layout dimensions of the accelerometer

Parameter	Value	Parameter	Value
W_1 (μm)	18	L_2 (μm)	2360
W_2 (μm)	2200	L_3 (μm)	2000
W_3 (μm)	20	L_4 (μm)	2020
W_4 (μm)	16	R_1 (μm)	24
L_1 (μm)	1050	N_1	52

The ideal process parameters are given in Table 2. T_1 is the thickness of the proof mass, T_2 is the thickness of the Al electrodes, D_1 is the distance between the bar electrodes and the Al electrodes, and D_2 is the etched trench depth.

Table 2 Ideal process parameters

Parameter	Value	Parameter	Value
T_1 (μm)	308.5	D_1 (μm)	1
T_2 (μm)	0.5	D_2 (μm)	60

With values given in Tables 1 and 2, the weight of the proof mass m is

$$m = \rho_{\mathrm{Si}}(W_2 L_2 T_1 - N_1 W_3 L_3 D_2), \tag{1}$$

where ρ_{Si} is the density of silicon. Spring constant K_x can be written as

$$K_x = \frac{N_2 E(2L_1 + \pi R_1) W_1^3 T_1}{2(2L_1^4 + 4\pi R_1 L_1^3 + 24R_1^2 L_1^2 + 6\pi R_1^3 L_1 + 3\pi^2 R_1^4 - 24R_1^4)}, \tag{2}$$

where N_2 is the number of spring beams, and E is Young's modulus. The mechanical resonant frequency f_x can be written as

$$f_x = \frac{\omega_x}{2\pi} = \frac{\sqrt{K_x / m}}{2\pi}. \tag{3}$$

For an ideal differential sensing capacitor pair C_{s}, sensing capacitors C_{s1} and C_{s2} can be written as

$$C_{\mathrm{s}} = C_{\mathrm{s1}} = C_{\mathrm{s2}} = \frac{\varepsilon N_1 W_4 L_3}{2D_1}, \tag{4}$$

where ε is the permittivity of air. And the rest capacitors C_{r1} and C_{r2} are

$$C_{\mathrm{r}} = C_{\mathrm{r1}} = C_{\mathrm{r2}} = \frac{\varepsilon N_1 (W_4 L_4 - 0.5 W_4 L_3)}{D_1}. \tag{5}$$

The mechanical sensitivity of the accelerometer is derived from the differential value of Eq.(4):

$$S_{\mathrm{m}} = 2\frac{\mathrm{d}C_{\mathrm{s}}}{\mathrm{d}(0.5W_4)} = \frac{2\varepsilon N_1 L_3}{D_1}. \tag{6}$$

Results of the above parameters calculated with values given in Tables 1 and 2 are summarized in Table 3. The actual values of these parameters will differ because of the process errors. This will be discussed in Sections 3 and 4.

Table 3 Calculated parameters for the accelerometer

Parameter	Value	Parameter	Value
m (kg)	3.44×10^{-6}	C_{s} (pF)	7.36
K_x (N/m)	476	C_{r} (pF)	0.12
f_x (Hz)	1872	S_{m} (fF/μm)	1842

IMPROVED PROCESS FLOW

Fig.3 shows the process flow for the previous prototype.

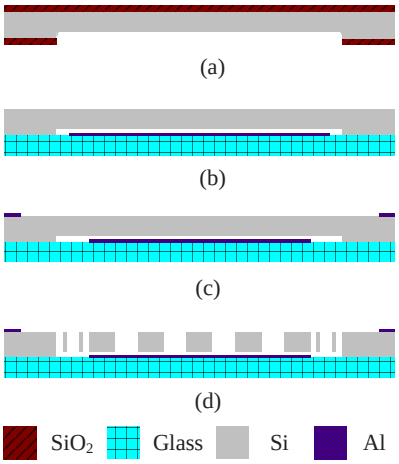

Fig.3 Process flow for the previous prototype
(a) A single crystal (100) silicon wafer is etched at the back by anisotropic wet etching to form the gap between the proof mass and the Al electrodes; (b) It is anodic bonded with glass which has sputtered Al electrodes on the silicon surface; (c) Al pads on the bonded wafer are formed by wet etching after sputtering Al; (d) The structure and bar trenches are released together using DRIE

The alignment mark at the back of the silicon wafer can be seen through the transparent glass; thus, accuracy of the alignment is assured for the silicon-glass bonding. The main alignment error of the electrodes comes from the last patterning for DRIE. Since the alignment marks of the Al electrodes on the glass are under the silicon wafer, the top-bottom alignment method is needed for the last patterning. And the tolerance of the top-bottom alignment step directly decides the accuracy of the alignment of the electrodes, which is about 1 μm.

The lower part of the structure is etched unexpectedly due to the footing effect in DRIE. This is aggravated when the etched part has nonuniform geometry, because the etching rate of DRIE has a strong dependency on the trench width (Ishihara *et al*., 1999). The space between bars is smaller than the structure clearance, and thus the etching rate of trenches is slower than the structure release rate. As a result, DRIE will have to continue working for the trenches to be cut through after the structure is released, which aggravates lateral etching on structure sidewalls, as is shown in Fig.4a. Lateral etching due to the footing effect spreads over most of the sidewall area. Even though DRIE stops right after the trenches are cut through, bar surfaces can still be affected by the reflected ion, resulting in a rough surface.

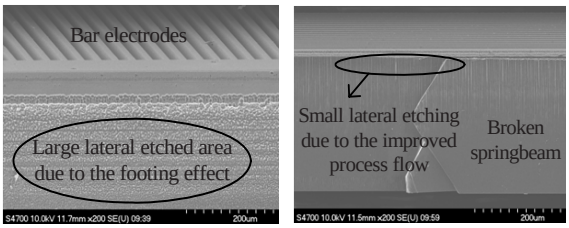

Fig.4 SEM photos showing the footing effect on structure sidewalls. (a) Previous prototype; (b) Current prototype

An effort is made to reduce the footing effect and improve the device quality. The improved process flow is shown in Fig.5.

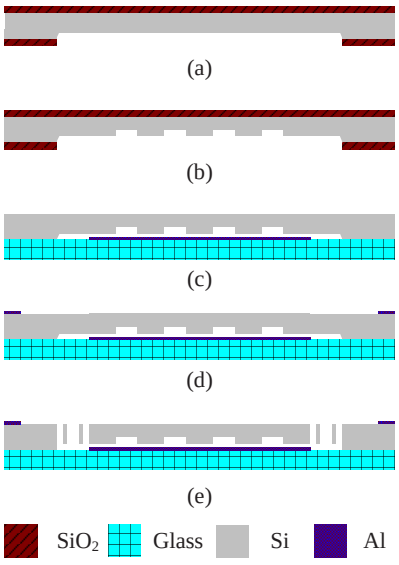

Fig.5 Improved process flow
(a) A single crystal (100) silicon wafer is etched at the back by anisotropic wet etching to form the gap between the proof mass and the Al electrodes; (b) The bar trenches are etched at the back of the silicon by DRIE with a depth of 60 μm, which is about one-fifth of the silicon thickness; (c) Al pads on silicon are formed by wet etching after sputtering Al on the silicon surface; (d) The silicon wafer is anodic bonded with a glass that has sputtered Al electrodes on it; (e) The structure is released using DRIE

In this case, the alignment accuracy of electrodes depends on the alignment tolerance of the silicon-glass bonding process, instead of the misalignment for the last patterning for DRIE, where the top-bottom alignment method is needed. It is because the bars at the back of silicon are formed before the silicon-glass bonding process. Since the glass is transparent, alignment marks at the back of the silicon can be directly seen through the glass, and no top-bottom alignment method is needed for the bonding process. The tolerance for the electrode alignment is about 1 μm.

Compared to the previous process flow, the bar trenches are etched before anodic bonding and only about one-fifth of the silicon thickness is etched. This comes along with a few advantages.

Firstly, the proof mass is increased greatly as the trench depth is only one-fifth of the previous one and thus results in a lower Brownian noise floor. In this case, the proof mass is increased by 54% as compared with the condition under which the trenches are etched through. Secondly, the bar electrode surface will not be affected by DRIE, so a clean surface can be achieved. Thirdly, this greatly reduces the etching area during the last DRIE process. Therefore, it is easier to design layout patterns with good geometric uniformity. As a result, the whole wafer is released almost at the same time, and the footing effect is lowered greatly. Fig.4b shows that the lateral etching on the sidewall due to the footing effect is markedly reduced with the improved process flow. This can be compared with the sidewall of a previous prototype (Fig.4a). Thus, the device quality and yield rate are both improved. Furthermore, as the depth of the trenches is reduced, the aspect ratio of the bar structure is reduced as well; i.e., either less demanding fabrication technology can be used to etch the trenches or more bars with a more narrow width within the same area can be designed to increase the mechanical sensitivity of the accelerometer.

An overview of the fabricated accelerometer is shown in Fig.6. The main dimension error of the device comes from the last DRIE process, where thick photoresist is used as the mask for the etching. After post-baking for the developed photoresist, the edges of the thick photoresist are not ideally vertical; thus, the photoresist near the edge is thinner than expected, implying that the silicon under the photoresist edge area is etched. Hence, the actual width of the spring beams is smaller than the layout value. The measured width of the fabricated spring beams is about 14 μm, about 4 μm smaller than the layout value. It implies that the actual resonant frequency is smaller than that predicted with the layout value. This will be further discussed in the next section.

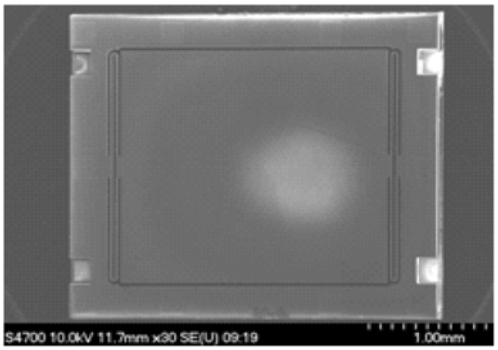

Fig.6 SEM photo of a fabricated prototype

TEST RESULTS

The frequency response of a prototype was tested by applying electrostatic forces with different frequencies to the proof mass and recording the corresponding output of the sensing capacitor pair. Because the bar electrodes and the fixed electrodes were partially overlapped, an electrostatic force in the lateral direction was induced to make more overlapped area for the electrodes when voltages were applied. Push-pull drive voltages were added to the two electrodes fixed on the glass substrate to perform the lateral electrostatic force. V_{dc} is the DC component of the drive voltage; V_{ac} is the AC component. The electrostatic force F_e can be written as

$$F_e = \frac{2N_1 \varepsilon L_3 V_{dc} V_{ac}}{D_1}, \tag{7}$$

which is proportional to the number of bars, the length of the trenches, and the amplitudes of the AC and DC components. The capacitor variance due to the electrostatic force was converted to an electrical signal with a capacitance-voltage circuit and then recorded by a digital oscilloscope. Normalized results of the frequency response are shown in Fig.7.

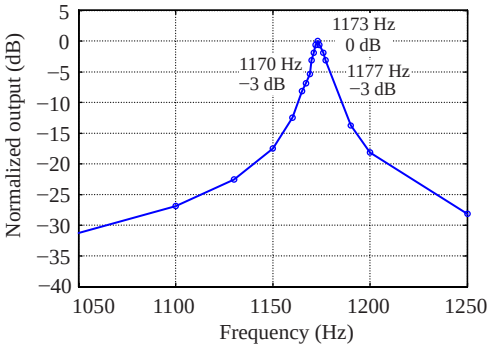

Fig.7 Frequency response under lateral electrostatic force

The measured resonant frequency was 1173 Hz with a quality factor of about 160, while the result predicted with layout dimensions was 1873 Hz. This is mainly because the width of the fabricated spring beams was about 4 μm smaller than the layout value. Substituting the measured width into Eqs.(2) and (3), the theoretical resonant frequency of the accelerometer is 1283 Hz, which is close to the tested value.

The damping coefficient C_x predicted by the Couette damping model (Cho *et al.*, 1994) can be written as

$$C_x = \mu \frac{A_x}{D_1}, \tag{8}$$

where μ is the coefficient of viscosity and A_x is the area of the proof mass. The calculated value is 9.35×10^{-5} kg/s. The accelerometer quality factor

$$Q = \frac{m\omega_x}{C_x} \tag{9}$$

as predicted by the Couette damping model (Cho *et al.*, 1994) is 260, which is slightly higher than the tested value of 160. The reason is that the proof mass does not have a perfect flat surface and sidewalls of the trenches also suffer air damping. It complies with the low damping scheme.

Brownian noise for the accelerometer is (Boser and Howe, 1996)

$$a_{\mathrm{BN}} = \sqrt{4K_{\mathrm{B}}T\omega_x / (mQ)}, \tag{10}$$

where K_{B} is the Boltzmann constant and T is the thermodynamic temperature. a_{BN} is calculated to be 0.47 μg/Hz$^{1/2}$.

The interface circuit for the prototype is shown in Fig.8. The two sensing capacitors, C_{s1} and C_{s2}, are amplitude modulated to a high frequency input sine wave by two symmetric integrators. Then the differential AM signals are amplified with an instrument amplifier, and the amplified signal is afterwards demodulated with the input sine wave and filtered with a low-pass filter before output.

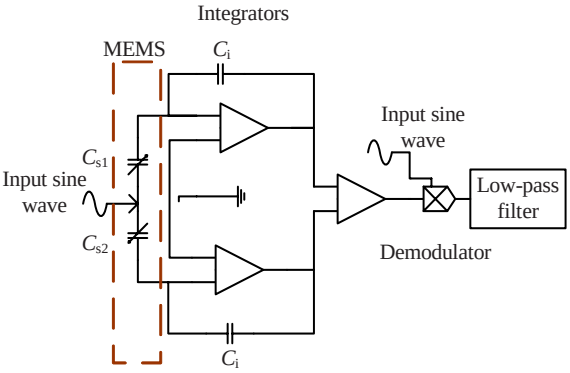

Fig.8 Interface circuit for the accelerometer

The electrical sensitivity of the interface circuit is

$$S_{\mathrm{e}} = \frac{V_{\mathrm{out}}}{\Delta C} = \frac{V_{\mathrm{s}} C_1 G_2}{C_{\mathrm{i}}}, \tag{11}$$

where V_{out} is the output voltage of the circuit, ΔC is the capacitor difference of the differential capacitor pair, V_{s} is the amplitude of the input sine wave, C_{i} is the integrator capacitor, G_1 is the gain of the instrument amplifier, and G_2 is the gain of the low-pass filter. Thus the total sensitivity of the accelerometer is written as

$$S_{\mathrm{acc}} = \frac{g}{\omega_x^2} S_{\mathrm{m}} S_{\mathrm{e}}, \tag{12}$$

where g is the acceleration of gravity. For values given in Table 4 the value calculated with the tested resonant frequency is 89.7 mV/g.

Table 4 Parameters for the interface circuit

Parameter	Value	Parameter	Value
V_{s} (mV)	450	G_1	6
C_{i} (pF)	10	G_2	1

A linearity test was performed on a circular dividing table. Accelerometer output data were taken by an Agilent34401A digital multimeter every 10°. Test results are shown in Fig.9, and the output offset has been eliminated. The scale factor was 71.34 mV/g, smaller than that predicted by Eq.(12). This is because the rest capacitor pair C_r bears an opposite sensitivity against the differential capacitor pair C_s. Output residual after a linear fit for each input point has also been shown in this figure, and the maximal residual value was about 0.6 mV, equivalent to an acceleration of 8.4 mg. The results show very good linearity, which results from the linear capacitor sensing scheme of sensing via varying the overlapped area instead of the gap.

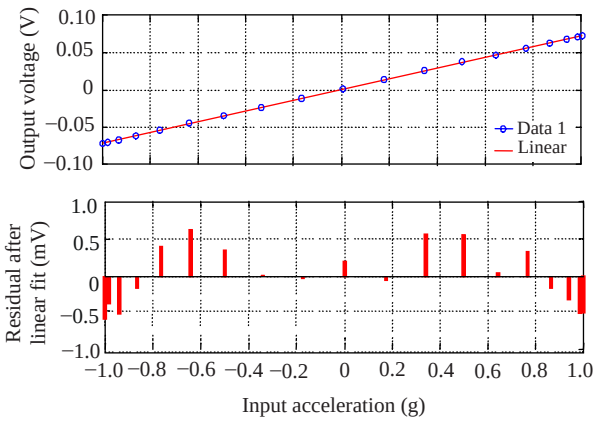

Fig.9 Linearity test for the accelerometer

A bias stability test was carried out by taking zero output data for 1 h with an Agilent 34401A digital multimeter and the Allan deviation for the data is shown in Fig.10.

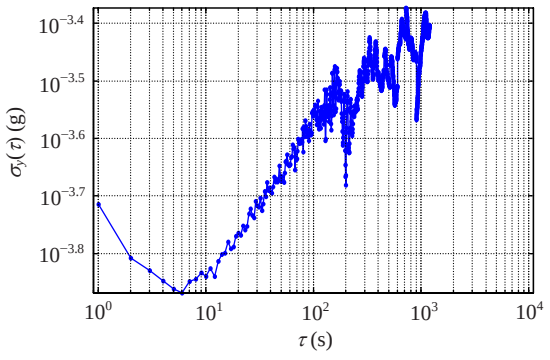

Fig.10 Allan deviation for the accelerometer at room temperature and atmospheric pressure

Both Brownian noise of the device and electronic noise of the interface circuit affect the bias stability of the output. The Allan deviation showed a random bias of 130 μg at an averaging time of around 6 s. Brownian noise of the accelerometer was 0.47 μg/Hz$^{1/2}$, and the low-pass filter bandwidth of the interface circuit was 100 Hz, so the root mean square (rms) power within the bandwidth of Brownian noise was 4.7 μg, which was only 5.6% of the tested random bias. This means that the bias stability was not restricted by Brownian noise in this case. Instead, it was limited by electronic noise of the interface circuit. Besides, fluctuations in external and internal environments such as temperature also have an effect on the bias stability. This indicates that the performance of the device can be further optimized by lowering the electronic noise of the interface circuit.

CONCLUSION

A bulk micromachined in-plane capacitive accelerometer is fabricated with an improved process flow. Lateral etching at sidewalls caused by the footing effect is greatly reduced and the proof mass is increased by 54%. Device quality and yield rate are both improved. The tested frequency response of a prototype complies with the low damping design with a quality factor of 160. Linearity from −1 g to 1 g is tested and the results show very good linearity, and the maximal residual value after linear fit is 8.4 mg. The Allan deviation for zero output data in 1 h shows a random bias of 130 μg at an averaging time of around 6 s.

ACKNOWLEDGEMENTS

The authors would like to thank Shanghai Institute of Microsystem and Information Technology for the fabrication support of MEMS accelerometers.

References

Boser, B.E., Howe, R.T., 1996. Surface micromachined accelerometers. *IEEE J. Solid-State Circuits*, **31**(3):366-375. [doi:10.1109/4.494198]

Bustillo, J.M., Howe, R.T., Muller, R.S., 1998. Surface micromachining for microelectromechanical systems. *Proc. IEEE*, **86**(8):1552-1574. [doi:10.1109/5.704260]

Chae, J., Kulah, H., Najafi, K., 2004. An in-plane high-sensitivity, low-noise micro-g silicon accelerometer with CMOS readout circuitry. *J. Microelectromech. Syst.*, **13**(4):628-635. [doi:10.1109/JMEMS.2004.832653]

Chen, Y., Jiao, J., Dong, L., Xiong, B., Che, L., Li, X., Wang, Y., 2003. Micromachined bar-structure gyroscope with high Q-factors for both driving and sensing mode at atmospheric pressure. *Sensors, Proc. IEEE*, **1**:461-465. [doi:10.1109/ICSENS.2003.1278980]

Cho, Y.H., Pisano, A.P., Howe, R.T., 1994. Visous damping model for laterally oscillating microstructures. *J. Microelectromech. Syst.*, **3**(2):81-87. [doi:10.1109/84.294325]

Ishihara, K., Yung, C.F., Ayon, A.A., Schmidt, M.A., 1999. Inertial sensor technology using DRIE and wafer bonding with interconnecting capability. *J. Microelectromech. Syst.*, **8**(4):403-408. [doi:10.1109/84.809054]

Jiang, X., Wang, F., Kraft, M., Boser, B.E., 2002. An Integrated Surface Micromachined Capacitive Lateral Accelerometer with 2 μG/√Hz Resolution. Solid-State Sensor, Actuator and Microsystems Workshop, p.202-205.

Kovacs, G.T.A., Maluf, N.I., Petersen, K.E., 1998. Bulk micromachining of silicon. *Proc. IEEE*, **86**(8):1536-1551. [doi:10.1109/5.704259]

Wang, Y., Guo, Y., Zhang, H., 2007. Modeling and Simulation of Footing Effect in DRIE Process. Proc. 7th IEEE Int. Conf. on Nanotechnology, p.1135-1138. [doi:10.1109/NANO.2007.4601383]

Weigold, J.W., Najafi, K., Pang, S.W., 2001. Design and fabrication of submicrometer, single crystal Si accelerometer. *J. Microelectromech. Syst.*, **10**(4):518-524. [doi:10.1109/84.967374]

Yazdi, N., Najafi, K., 1997. An All-silicon Single-wafer Fabrication Technology for Precision Microaccelerometers. Proc. Int. Conf. on Solid-State Sensors and Actuators, p.1181-1184. [doi:10.1109/SENSOR.1997.635416]

Zheng, X., Cao, X., Zheng, Y., Luo, S., Wang, Y., Jin, Z., 2008. Study of a novel micromachined capacitive accelerometer. *Chin. J. Sens. Actuat.*, **21**(2):226-229 (in Chinese).